



HAL
open science

Experimental and numerical investigations of the flow around an oar blade

Alban Leroyer, Sophie Barré, Jean-Michel Kobus, Michel Visonneau

► **To cite this version:**

Alban Leroyer, Sophie Barré, Jean-Michel Kobus, Michel Visonneau. Experimental and numerical investigations of the flow around an oar blade. *Journal of Marine Science and Technology*, 2008, 13 (1), pp.1-15. 10.1007/s00773-007-0256-7 . hal-00699499

HAL Id: hal-00699499

<https://hal.science/hal-00699499>

Submitted on 18 Jan 2022

HAL is a multi-disciplinary open access archive for the deposit and dissemination of scientific research documents, whether they are published or not. The documents may come from teaching and research institutions in France or abroad, or from public or private research centers.

L'archive ouverte pluridisciplinaire **HAL**, est destinée au dépôt et à la diffusion de documents scientifiques de niveau recherche, publiés ou non, émanant des établissements d'enseignement et de recherche français ou étrangers, des laboratoires publics ou privés.



Distributed under a Creative Commons Attribution - NonCommercial 4.0 International License

Experimental and numerical investigations of the flow around an oar blade

Alban Leroyer · Sophie Barré · Jean-Michel Kobus
Michel Visonneau

Abstract This article aims at verifying the capabilities of a Reynolds–Averaged Navier–Stokes Equations (RANSE) solver (ISIS-CFD, developed at the Fluid Mechanics Laboratory of Ecole Centrale de Nantes [LMF]) to accurately compute the flow around an oar blade and to deduce the forces on it and other quantities such as efficiency. This solver is structurally capable of computing the flow around any blade shape for any movement in six degrees of freedom, both when the blade pierces the free surface of the water and when it does not. To attempt a first validation, a computation was performed for a simplified case chosen among those for which experimental results are available at LMF. If results prove satisfactory for a simplified blade shape and for a movement that respects the main characteristics of blade kinematics, then the solver could be used for real oars and more realistic kinematics. First, the experimental setup is considered, and the objectives, methodologies, and procedures are elucidated. The choice of the test case for numerical validation is explained, i.e., a plane rectangular blade with a constant immersion and a specified movement deduced from analogy with tests on propellers. Next, the numerical

framework is presented and the Navier–Stokes solver and methods for handling multifluid flows and moving bodies are described. Lastly, numerical results are compared with experimental data, highlighting an encouraging agreement and proving the relevance and the complementarity of both approaches.

Key words Rowing · Oar blade · Free-surface flow · Navier–Stokes solver

1 Introduction

Fluid mechanics is a scientific field that plays a key role in nautical sports, mostly in complex situations. This is particularly true for rowing, for which fluid flow knowledge is required twice: once around the boat hull and again around the oar blades. Moreover, all the phenomena involved in rowing (the movement of rowers, the forces acting on the oars, and the behaviour and resistance of the hull) strongly interact. Consequently, the only means of analysing and understanding rowing is to use dynamic simulations. Therefore, since 1998 the Fluid Mechanics Laboratory of Ecole Centrale de Nantes (LMF) has developed a simulator for a complete boat–oarsmen–oars system. This tool constitutes a means of forging a permanent and operational synthesis of the research and studies on rowing. The accuracy of simulations evolves according to the progress in results and validations. The relevance and the applicability of our simulator required a thorough study of the phenomena involved in oar propulsion. Large variations in speed added to the heave and pitch of the boat induced by the movement of oarsmen during the rowing stroke, make the flow around rowing boats difficult to investigate.

A. Leroyer (✉) · M. Visonneau
Laboratoire de Mécanique des Fluides, Ecole Centrale de
Nantes, B.P. 92101, 1 rue de la Noë, 44321 Nantes, France
e-mail: alban.leroyer@ec-nantes.fr

S. Barré
Ecole Nationale de Voile, Quiberon, France

S. Barré · J.-M. Kobus
Laboratoire de Mécanique des Fluides, Equipe Hydrodynamique,
Navale et Génie Océanique, Ecole Centrale de Nantes, Nantes,
France

However, the flow around an oar blade appears far more complex and has been far less studied.

Most authors adopt the very simple model suggested by Wellicome¹ to evaluate the force on oar blades and to develop considerations on optimisation of oar setting and rowing style. This model supposes that the force is perpendicular to the blade and proportional to the square of the normal component of the instantaneous absolute velocity calculated at the centre of the blade. This quasi-static model is dimensionally consistent, but the coefficient of proportionality is never precisely specified. Some computational fluid dynamics (CFD) studies have been carried out using Videv² to calculate this coefficient in a two-dimensional case without a free surface, but this simplified configuration is too far from the specificity of flow around oar blades to be helpful.

To improve the evaluation of efforts on blades induced by such a complex flow, only an experimental approach seemed to be feasible until a few years ago. To perform such experiments, the LMF built a sophisticated device for testing blades at reduced scale and also for testing real scull oars in its towing tank. Nevertheless, during the past decade, thanks to the growth of storage capacity and computing power, CFD tools have become no longer limited to simple physical problems and have significantly enlarged their field of applications. The in-house Reynolds–Averaged Navier–Stokes Equations (RANSE) solver ISIS-CFD integrates new physical features to deal with increasingly realistic applications, such as moving bodies and complex free-surface flows. Thus, it seemed to us that the time had come to compare the results of CFD simulations with experimental results on such a complex configuration. As a result, initial simulations have been recently performed. To explain our approach to the problem and to comment on the results are thus the main goals of the present article, which is devoted to the experimental and numerical aspects of oar blade hydrodynamics.

First, Sect. 2 describes the experimental approach, the procedure, and the aims of such a study. The experimental configuration chosen for comparison with the numerical results is one of those tested during a testing campaign, the aim of which was to build a model of hydrodynamic forces on a blade as a function of the movement in the water and the geometric characteristics. To discuss this modelling is not the subject of this article; nor is it intended to make any conclusions about real rowing styles. Here, the test bench and the associated procedures are described, so that the reader can evaluate the degree of confidence which can be afforded to the experimental results. The blade chosen for the study is the reference blade of systematic tests, that is to say, a

plane rectangular blade with a rigid shaft moving with analytical kinematics defined by only two parameters. The reasons for this selected configuration for numerical validation conclude Sect. 2.

In Sect. 3, the numerical methods are considered and the main features of the RANSE solver are given. Special attention is paid to the numerical treatment of the moving grid in the Navier–Stokes equations. This point needs to be addressed as soon as body motion is encountered. Next, the simulations performed for this initial study on an oar blade are detailed in terms of meshes, boundary conditions, law of motion. The time evolution of the free surface is lastly described. In Sect. 4, comparisons between available experimental measurements and simulations are shown. Forces and torque are considered first. A comparison of experimental and numerical evaluation of efficiency completes the discussion. Lastly, conclusions highlight the complementarity of both approaches and the perspectives of such research.

2 Experimental approach

2.1 General methodology of the test campaigns

Instrumented boats are now commonly used to measure the motions and forces acting on oar blades. Such tests have already been performed, in particular at LMF. They have the advantage of working directly on a realistic configuration, but the complexity of in-situ measurements, which involve numerous and sometimes not precisely controlled parameters, does not allow adequate precision and repeatability to build or validate models of forces on blades. For example, it is technically difficult to measure the hydrodynamic force on a blade, and the position (or velocity) of blades is not precisely known because of oar flexibility and variable immersion. Thus, in-situ measurements have been preferentially used until now for comparative analysis and for global validation of rowing simulations. Another approach is to reproduce as well as possible the movements of blades in a towing tank. This technique permits the separation of the propulsive device (the oar) from the motor (the oarsman) and from the boat, as it is done for propellers. Such a system was designed at LMF³ for testing real oars or models of blades at a reduced scale with a rigid shaft. The system generates a simplified rowing stroke but with good control of the parameters and with accurate reproducibility. In order to avoid a complex mechanism, the blades always remain in the water. To limit the consequences of this feature, it is possible to impose a movement (denoted the neutral movement) calculated to minimise the drag on the blade before the catch angle of

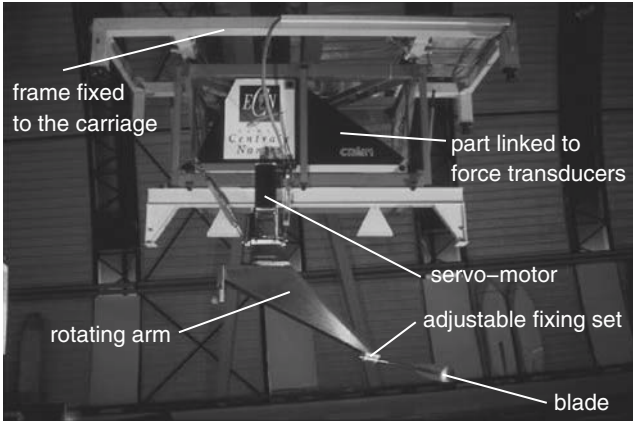


Fig. 1. Photograph of the rowing device

the real stroke. This technique introduces supplementary parameters such as the neutral motion duration and the transition phase duration (the catch). In order to perform systematic tests, we also defined simplified movements with only two kinematic parameters specified under efficiency considerations, as described later.

2.2 Experimental device description

The device is a six-component dynamometer equipped with a servomotor and a mechanism which reproduces accurately and repeatably the rotation of the oar blade in the water (see Fig. 1). The servomotor is a brushless motor with high specific power. Reduction of the rotation is done with a gear box associated with two pulleys and a belt. The motor has a numerical control system which ensures that the motor conforms to a given displacement (or speed) reference signal. The dynamometer allows the servomotor and the transmission mechanism to be fixed directly on to the measuring device. This arrangement eliminates the influence of interior transmission efforts and allows the measurement of the hydrodynamics force on the blade, corrupted only by some parasitic effects. The device was fixed to the towing tank carriage and the speed of translation was constant during the stroke. Immersion adjustment was set by shifting the dynamometer support up and down. The vibrations of the carriage excite the natural frequencies of the dynamometer. From analysis of some in-situ measurements on a skiff, we deduced that the amplitude spectrum of the forces on oars has no significant value higher than 7Hz, so we designed the device to have natural frequencies higher than 15Hz. To achieve these favourable conditions, the measuring part of the dynamometer and the rotary arms were built from carbon fibre. The test bench measured forces and moments acting on the oar in conjunction with the characteristics of the predefined movements, but deformation of the oar

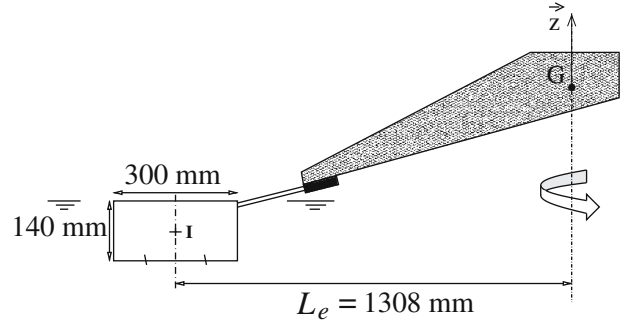


Fig. 2. Definition of the blade. G , centre of gravity of the rotating system; I , centre of the blade; L_e , outboard lever

shaft and deflection of the blade were not measured. As the position of the blade in the water has to be precisely known for numerical validation, we chose to use results obtained with the bench equipped with a rotating arm suitable for blades of reduced scale (see Figs. 1 and 2). Along with the arm, the blade shaft is very short and was made of monolithic carbon to obtain great rigidity. It was fastened on the rotary arm using a device that makes it possible to adjust the external lever, the inclination of the oar shaft and the angle of the blade in the vertical direction.

2.3 Experimental procedures

Before each run, the centre of gravity was adjusted to lie on the rotation axis and the inertial characteristics were measured. The inertial effects consisted of moments only, because the translation speed was constant. We also measured the aerodynamic forces on the device. The numerical file of reference signals used by the control system was calculated with a specific program that computed the different phases of the blade rotation during the experiment. A run proceeded in four steps. The oar blade was initially oriented at 0° . The carriage was then accelerated to the desired speed, and then ran at this constant speed. Then, the blade followed the specified trajectory up to an angle of 180° before the carriage stopped. The measurement processing was done as follows. The device produced eight analogue voltage outputs: six outputs came from force transducers in the dynamometer and the two other outputs were the angular position and velocity of the servomotor. These signals were sampled and stored. The six components of forces and moments in the dynamometer frame of reference were calculated at each sample time using a calibration and coupling matrix. Next they were filtered to eliminate noise and forces induced by vibrations in the dynamometer. The angular position and velocity were also sampled and filtered. Finally, we introduced corrections to eliminate the inertial effects induced by experimental proce-

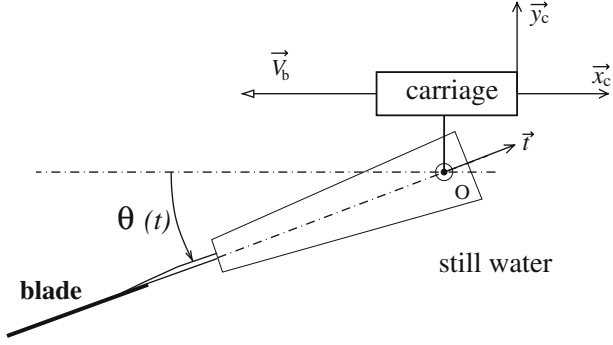


Fig. 3. Top view of the experimental configuration

dures so as to obtain only the hydrodynamic forces and moments. The different stages are described below.

Sampling and measurement acquisition. For measurements acquisition, we use an A/D converter card controlled by an advanced program. This program permits the definition of acquisition sequences and stored them. The sampling frequency was chosen to be 500 Hz to avoid using an anti-aliasing filter.

Filtering. The filtering method consisted of a low-pass windowing spectrum followed by a reconstitution of the signal by applying an inverse Fourier transform. This technique did not induce any phase shift between measured signals. A band of frequency between 7 and 15 Hz having very low spectral power allowed low-pass filtering to be performed with good precision and with few induced perturbations in the pass band.

Pre-processing. This procedure consisted first in ordering and storing raw data and filtered data, and second in correcting data using inertial and aerodynamic effects.

Measurement exploitation. First, the physical parameters used for analysis and modelling were computed, and second, kinematic data and forces measured in the dynamometer axis were used to calculate the forces in a different axis (e.g., the blade axis or the relative incidence of water). Finally, hydrodynamic coefficients, the instantaneous driving force, the effective power, and the instantaneous and global efficiencies were evaluated.

2.4 Blade kinematics and efficiency considerations

To begin with, some notations were defined as follows and are represented in Figs. 2–4.

Geometry and kinematics

- $(\bar{x}_c, \bar{y}_c, \bar{z}_c)$: frame of reference linked to the carriage (or boat), with \bar{z} upward and the motion of the carriage directed towards $-\bar{x}_c$

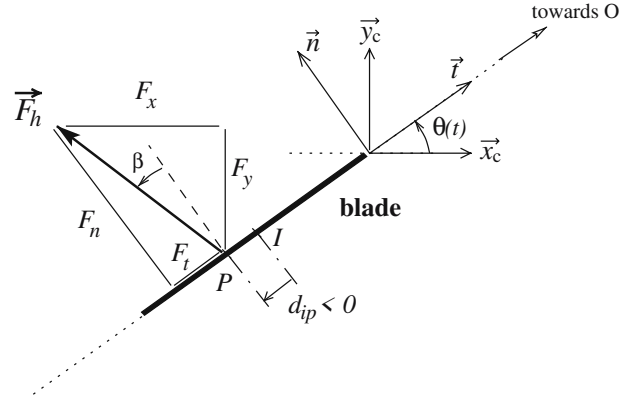


Fig. 4. Definition of the axes

- $(\bar{t}, \bar{n}, \bar{z})$: frame of reference linked to the blade, with \bar{t} the horizontal vector tangent to the blade directed towards the rotation axis
- L_e : outboard lever (>0), i.e., the distance between the rotation axis (O, \bar{z}) and I , the centre of the blade surface
- $\theta = (\bar{x}_c, \bar{t})$: the angle between the shaft and the translational boat velocity
- β : the angle between hydrodynamic force \bar{F}_h and \bar{n} , the vector perpendicular to the blade
- $V_b = |\bar{V}_b| = -\bar{V}_b \cdot \bar{x}_c$: the boat velocity (>0).

Components of horizontal hydrodynamic force \bar{F}_h and the torque in different axes of reference (see Fig. 4)

- F_x, F_y : in the dynamometer (or boat) axis
- F_t, F_n : in the shaft axis,
- M_z : the component of the hydrodynamic torque applied about (O, \bar{z}).

The instantaneous efficiency η is defined as the ratio of the useful power to the delivered power:

$$\eta = \frac{F_x V_b}{M_z \dot{\theta}} \quad (1)$$

Let us denote the centre of the blade I , and the point where the resultant fluid force \bar{F}_h acts at each instant P (see Fig. 4). Then, Eq. 1 can be formulated as:

$$\eta = \frac{-|\bar{F}_h| \cdot \sin(\theta + \beta) \cdot V_b}{(\overline{OI} + d_{ip}) \cdot |\bar{F}_h| \cdot \cos(\beta) \dot{\theta}} = \frac{\sin(\theta + \beta) \cdot V_b}{(L_e - d_{ip}) \cdot \cos(\beta) \dot{\theta}}, \quad (2)$$

where d_{ip} is the algebraic distance between I and P projected on the oriented shaft axis (O, \bar{t}).

Note that $M_z = -(L_e - d_{ip}) \cdot F_n = (L_e - d_{ip}) \cdot (F_x \sin \theta - F_y \cos \theta)$. So, we can deduce:

$$d_{ip} = L_e - \frac{M_z}{F_x \sin \theta - F_y \cos \theta} \quad (3)$$

By extending Eq. 2, we can thus obtain:

$$\eta = \frac{V_b \sin \theta}{L_e \dot{\theta}} \left(1 + \frac{\tan \beta}{\tan \theta} \right) \left(\frac{1}{1 - d_{ip}/L_e} \right) = \eta_0 \cdot \eta_f \cdot \eta_p \quad (4)$$

This defines three components of efficiency:

$$\begin{aligned} \eta_0 &= V_b \sin \theta / (L_e \dot{\theta}), & \eta_f &= (1 + \tan \beta / \tan \theta), \\ \eta_p &= 1 / (1 - d_{ip}/L_e) \end{aligned} \quad (5)$$

The efficiency component η_p , related to the centre of pressure, is close to unity since d_{ip} cannot be greater than half the length of the blade, i.e., quite small relative to L_e . The component η_f depends on the orientation β of the hydrodynamic force \vec{F}_h relative to the blade perpendicular \vec{n} . It is always unity when $\theta = \pi/2$. During the angular range of a real stroke (where θ can vary from about 40° through to 130°), β remains small and η_f is close to unity. Thus, the component η_0 appears to be the most significant component of the efficiency. Its value is close to that of η when F_x and M_z are maximum and it depends only on kinematics and on the characteristic length of the oar L_e .

By analogy with propellers, note that η_0 can be regarded as a kind of advance number that is representative of the incidence history. More precisely, if $\vec{V}_I = V_n \vec{n} + V_t \vec{i}$ is the velocity of the centre of the blade, we can define the pseudo-incidence of water, denoted i , as the angle of the opposite of \vec{V}_I relative to the tangent vector \vec{t} . Then we can write:

$$\tan i = \frac{L_e \dot{\theta} - V_b \sin \theta}{V_b \cos \theta} = \tan \theta \left(\frac{L_e \dot{\theta}}{V_b \sin \theta} - 1 \right) = \tan \theta \left(\frac{1}{\eta_0} - 1 \right) \quad (6)$$

The history of the pseudo-incidence i depends only on the angular position of blade and on η_0 . It can be noted here that during the possible phase of neutral movement (which corresponds to $\eta_0 = 1$ for a θ value less than the catch angle), the pseudo-incidence remains equal to zero. To define blade movements for systematic tests, we cannot reproduce real measured oar movements because these measurements are performed with oarsmen having different rowing styles and are not linked with reliable data on instantaneous boat speed. Furthermore, the high number of parameters that define this kind of movement makes the exploitation of test results difficult. We observed great disparities in the forces and moments curves according to chosen movement parameters. Con-

sequently, to perform systematic tests, we defined movements with two main parameters according to kinematics and energetic considerations. Wellicome,¹ and Pope⁴ after him, showed that the global efficiency of a stroke has a maximum value when the instantaneous efficiency is constant during the stroke. Wellicome emphasized that Betz used this argument originally in determining the optimum distribution of pitch for a propeller. So we decided to test oar blades with movements that make the component η_0 constant. This is the simplest way of keeping efficiency η almost constant during a wide part of the stroke (including the angular range of a real rowing stroke), since η_0 depends only on kinematics and geometry. Modelling of efforts will be done in this condition. This choice seems to be restrictive, but elite rowers search for optimum efficiency for a given power and their rowing style is probably close to one of constant efficiency. Then, if η_0 remains constant during the stroke, the definition of η_0 in Eq. 5 imposes the following condition:

$$\forall \theta, \dot{\theta} = K \sin \theta, \quad \text{with } K = \dot{\theta}_{max} \quad (7)$$

Thus, we have:

$$\eta_0 = \frac{V_b}{L_e K} \quad (8)$$

Consequently, systematic tests were performed for different pairs of parameters (K, η_0), the K value varying from 3 to 4 $\text{rad}\cdot\text{s}^{-1}$ and η_0 varying from 0.59 to 0.8. The boat (carriage) velocity was deduced from Eq. 8. By integrating Eq. 7, we obtain:

$$\theta_a(t) = 2 \operatorname{atan}[\exp(K(t-t_0))], \quad (9)$$

with t_0 the time where $\theta_a = \pi/2$. For $t = 0$, $\theta_a(0) \approx 2 \cdot \exp(-Kt_0)$ is very small but not zero (typically, $\theta_a(0) = 0.01^\circ$, $\dot{\theta}_a(0) \approx 7 \times 10^{-4} \text{ rad}\cdot\text{s}^{-1}$). Between $\theta = 0$ and $\theta_a(0)$, a brief linear junction with a slope value of $K \sin(\theta_a(0))$ is applied to reduce the velocity discontinuity at $\theta_a(0)$. The time offset $\Delta t = 1/K$ introduced by the linear junction is taken into account to generate the reference signal of rotation. When η_0 is constant ($\eta_0 = Cst$), according to Eq. 6 and Eq. 9, we see that the pseudo-incidence history $i(t)$ is completely defined by the characteristic efficiency (or advance number) η_0 and $K = \dot{\theta}_{max}$.

Figure 5 gives an example of the temporal evolution of θ for $K = 3$ ($t_0 = 3.1084\text{s}$). Figure 6 shows the deviation between the analytical angle θ_a and the measured value θ_m . Because of the a posteriori recalibration of the analytical law θ_a with measurements, which defines a corrected time t_0 and ensures that $\theta_m(t_0) = \theta_a(t_0) = \pi/2$, the

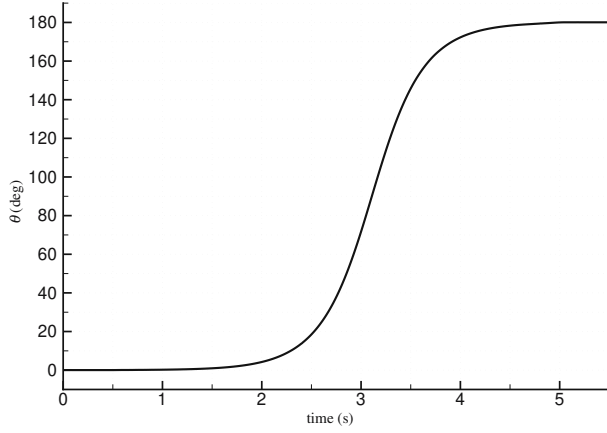


Fig. 5. Example of time evolution of the rotation angle θ

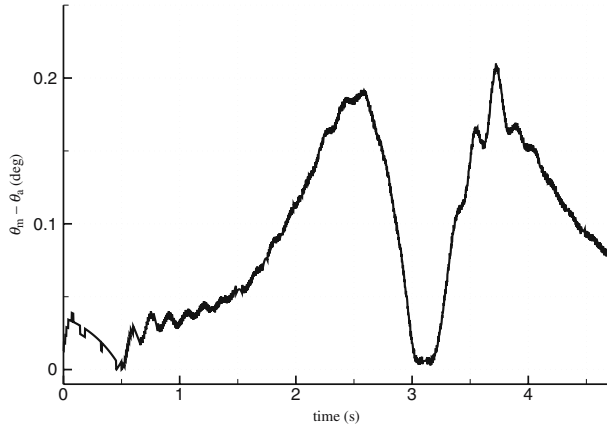


Fig. 6. Error between the measured angle (θ_m) and the analytically derived angle (θ_a)

error $\theta_m - \theta_a$ is then approximately zero around time t_0 . As we can see, the maximum deviation is quite small (about 0.2°). Analysis of the slope shows that the maximum error in terms of $\dot{\theta}$ does not exceed 0.7°s^{-1} in a range where $\dot{\theta}$ is always greater than 70°s^{-1} , giving a relative deviation of less than 1%. Thus, the analytical law has been used to prescribe the motion in CFD simulations instead of the measured data.

2.5 Choice of blade and experimental configuration for CFD comparison

Systematic tests were performed with six reduced-scale blades. In order to simplify the meshing of the blade, we chose the reference blade, that is to say, a planar rectangular blade (see Fig. 2), to compare measurements with numerical results. This choice does not alter the nature of the flow or the generality of comparisons. The parameters of the chosen movement were $\eta_0 = 0.5887$ and $K = \dot{\theta}_{max} = 3 \text{ rad}\cdot\text{s}^{-1}$. According to Eq. 8, the velocity of car-

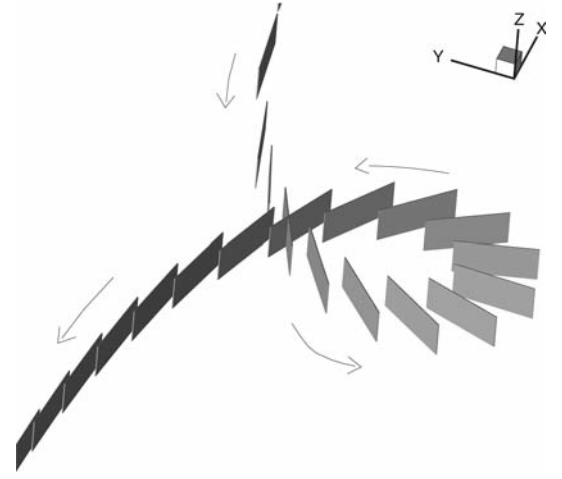


Fig. 7. Prescribed motion of the blade

riage was 2.31 ms^{-1} . The time evolution of θ is shown in Fig. 5 and the blade trajectory in Fig. 7. A particularly low efficiency with the blade close to the free surface was chosen because the flow is more perturbed than with highly efficient motion. With the aim being to validate the numerical approach, it seemed to be interesting to evaluate the capabilities of ISIS-CFD in calculating a flow with such severe conditions. If the agreement with experimental data turned out to be good for this case, we could be hopeful that the code, validated in such a complex configuration, would provide reasonable results when simpler configurations characterized with more realistic higher efficiency are studied.

Summary of hypothesis and simplifications

- The oar blade is a plane rectangle with a thickness of 3.5 mm (see Fig. 2).
- The area of the blade corresponds to a scull oar at scale 0.7 with the same aspect ratio.
- The blade chord is aligned with the shaft.
- The blade is vertical and its upper part remains at the level of the still free surface.
- The deformation of the shaft and blade is supposed to be negligible.
- The translation has a constant velocity.
- The movement is specified with a constant characteristic efficiency η_0 (or advance number), without a neutral phase at the beginning of the stroke.

It can be noted here that the specificity of the flow is mainly due to the unsteady rotation of the oar combined with the translation movement of the boat. It gives typical trajectories as shown in Fig. 7. As a consequence, despite the simplifications explained above, the flow

obtained around the blade is representative of the greater part of the physical phenomena that occur during a real oar stroke. This is a major point, since the objective is to validate numerical modelling of such a flow.

3 Numerical approach

3.1 Flow solver

The ISIS-CFD solver, developed by Equipe de Modélisation Numérique, the CFD Department of LMF, uses the incompressible unsteady Reynolds-averaged Navier–Stokes equations (URANS). The solver uses the finite-volume method to build the spatial discretization of the transport equations. The face-based method is generalized to unstructured meshes for which non-overlapping control volumes are bounded by an arbitrary number of constitutive faces. The velocity field is obtained from the momentum conservation equations and the pressure field is extracted from the mass conservation constraint, or continuity equation, transformed into a pressure equation. In the case of turbulent flows, additional transport equations for the modelled variables are solved in a form similar to the momentum equations and they can be discretized and solved using the same principles. Several turbulence models, ranging from the one-equation Spalart–Allmaras model,⁶ two-equation $k - \omega$ closures,⁷ to a full-stress transport $R_{ij} - \omega$ model,⁸ are implemented in the flow solver to take into account turbulence phenomena. Incompressible and non-miscible flow phases are modelled through the use of conservation equations for each volume fraction (or concentration) c_i of each phase i . Considering the incompressible flow of a viscous fluid under isothermal conditions, mass, momentum, and volume fraction conservation equations can be written as follow (using the generalized form of Gauss’ theorem):

$$\oint_S \bar{U} \cdot \bar{n} dS = 0, \quad (10a)$$

$$\begin{aligned} \frac{\delta}{\delta t} \int_V \rho \bar{U} dV + \oint_S \rho \bar{U} (\bar{U} - \bar{U}_d) \cdot \bar{n} dS \\ = \int_V (\rho \bar{g} - \bar{\nabla} P) dV + \oint_S (\mathbb{T} + \mathbb{T}_t) \cdot \bar{n} dS, \end{aligned} \quad (10b)$$

$$\frac{\delta}{\delta t} \int_V c_i dV + \oint_S c_i (\bar{U} - \bar{U}_d) \cdot \bar{n} dS = 0, \quad (10c)$$

where \mathcal{V} is the domain of interest, or control volume, bounded by the closed surface S moving at velocity \bar{U}_d with a unit normal vector \bar{n} directed outward. \bar{U} and P represent, respectively, the velocity and the pressure. \mathbb{T} and \mathbb{T}_t refer to the viscous and Reynolds stress tensors, whereas \bar{g} is the gravity vector. The time derivative fol-

lowing the moving grid is written $\delta/\delta t$. Whereas \mathbb{T}_t is determined according to the turbulence model used, \mathbb{T} follows the classical relation of a Newtonian fluid for incompressible flows.

The effective flow physical properties (viscosity μ and density ρ) are obtained from each of the phase properties (μ_i and ρ_i) using the following constitutive relations:

$$\rho = \sum_i c_i \rho_i, \quad \mu = \sum_i c_i \mu_i, \quad \sum_i c_i = 1 \quad (11)$$

Except for the convection terms and volumetric mass fluxes, the interfacial quantities q_f are rebuilt linearly from the quantities themselves and their available cell-centred gradients. Special attention has to be paid to face reconstructions of the volume fraction c_i . The challenge raised by the discretization of a transport equation for the concentration is the accurate modelling of the contact discontinuity, i.e., the free surface. In order to assume face-bounded reconstructions and to avoid unrealistic oscillations, the search for an acceptable compromise between accuracy and boundedness of $c_i \in [0, 1]$ is a key point.^{9,10} Moreover, the method must also preserve the sharpness of the interface through the transport equation (Eq. 10c).

These requirements are fulfilled by the inter-gamma differencing scheme (IGDS),¹¹ which introduces downwind differencing since compressive characteristics are required for accurate interface capturing. Through a normalized variable diagram (NVD) analysis,¹² this scheme enforces local monotonicity and the convection boundedness criterion (CBC).¹³ The main disadvantage of the IGDS scheme (and also of other compressive schemes) is a Courant number limitation, $Co < 0.3$ in multidimensional cases, known as the Courant–Friedrich–Levy (CFL) condition. The Courant number of any face is defined as follows:

$$Co = \Delta t \mathcal{F} / V \quad (12)$$

where \mathcal{F} is the total (positive) velocity flux through the considered face, V is the volume of the upwind cell, and Δt is the global time step of the temporal discretization. Therefore, the discretized time step has to be small enough to fulfil the CFL condition. It has been shown that the role played by the compressive property of the IGDS is fundamental to achieve a reliable simulation of the free surface.¹⁴

3.2 Body motion

To implement a body’s motion in a flow solver, the mesh must be adapted to the new position of the body over

time. In order to keep an appropriate grid, three complementary methods have been integrated (for further details, see Leroyer¹⁵):

- the pseudo-structure regriding procedure,
- the rigid transformation of the mesh,
- the analytical weighted regriding approach.

When the grid is moving, the so-called *space conservation law* must be satisfied:

$$\frac{\delta}{\delta t} \int_V dV - \oint_S \overline{U}_d \cdot \vec{n} dS = 0 \quad (13)$$

The mesh mobility is then taken into account in the equations of conservation with the grid velocity \overline{U}_d , or more precisely with the grid displacement velocity flux through each face S , denoted by $\mathcal{F}_{U_d}^S$. It is defined by:

$$\mathcal{F}_{U_d}^S = \int_S \overline{U}_d \cdot \vec{n} dS \quad (14)$$

For deformation techniques (pseudo-structure analogy and weighted regriding), this quantity is obtained by computing the exact volumes swept by cell faces during the time steps, which ensures that the discrete space conservation law is exactly satisfied.^{15,16} If a rigid transformation is also applied, its contribution to the displacement velocity fluxes can be exactly computed by using the parameters of the kinematic screw $\{\Omega, \vec{U}\}_{o_1}$ of the rigid transformation. Indeed, for each point M geometrically linked to this mesh, the velocity induced by the rigid displacement is defined by:

$$\overline{U}_d(M) = \overline{U}_d(O_1) + \vec{\Omega} \otimes \overline{O_1 M}$$

This property is used to generate a direct and exact calculation of the grid displacement velocity flux through each face S using the following:

$$\mathcal{F}_{U_d}^S = \int_S \overline{U}_d \cdot \vec{n} dS = \overline{U}_d(F) \cdot \vec{S}_f + \underbrace{\vec{\Omega} \cdot \int_S \overline{FM} \otimes \vec{n} dS}_{\mathcal{F}_r} \quad (15)$$

F denotes the centre of the face and \vec{S}_f the face vector. For a planar face (composed of three nodes), the definition of F is such that the integral of the term \mathcal{F}_r is strictly equal to zero. As far as non-planar faces are concerned (composed of more than three nodes), they are split into triangular faces, in which F is their common summit (see Fig. 8). By summing the contribution of each triangle making up the face, the term \mathcal{F}_r can be evaluated. In this way, the calculation of $\mathcal{F}_{U_d}^S$ is exact, whatever the face considered. As the motion is

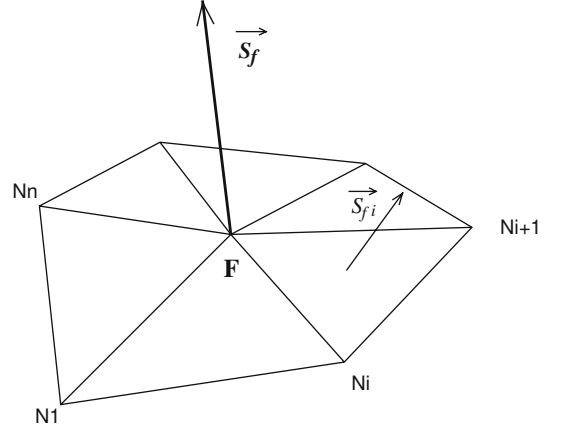


Fig. 8. Splitting of a non-planar face

a rigid displacement, we have for any point M geometrically linked to the mesh:

$$\text{div}(\overline{U}_d) = 0 \quad (16)$$

Applying the divergence theorem after integrating Eq. 16 yields:

$$\int_V \underbrace{\text{div}(\overline{U}_d(M))}_{=0} dV = \oint_{\partial V} \overline{U}_d(M) \cdot \vec{n} dS = \sum_{\text{faces}} \mathcal{F}_{U_d}^S = 0 \quad (17)$$

For simulations dealing with an isolated solid body in an infinite domain (as is the case here), only a rigid transformation is employed. This technique has no major effect on the computing time and enables motion of unlimited amplitudes in the physical space. Since there is no deformation, each cell conserves its volume. Therefore, the unsteady term $\delta V / \delta t$ is identically null for rigid displacement. Considering Eq. 17, the *space conservation law* is then exactly satisfied.

In the case of prescribed motions, at every time step, bodies are first displaced, then the mesh is regrided, and lastly the flow is solved. Hence, there is no real coupling, and this is because of the lack of fluid feedback on the body position. Since the motion is imposed here, the question of the resolution of the motion and of the coupling with the flow is not considered. For solved motions, further information is given by Leroyer¹⁵ and Leroyer and Visonneau.¹⁷

3.3 Characteristics of simulations

Three simulations were performed; their characteristics are summarized in Table 1. The first simulation was based on a coarse mesh of 120000 cells with an adaptive time step law to ensure the compressive property of the

Table 1. Characteristics of the configurations studied

Parameter	Sim1	Sim2	Sim3
Mesh name	M12e4	M14e5	M14e5
Cell number	120 000	1 400 000	1 400 000
Time law	Adaptive	Uniform ($\delta t = 0.005$ s)	Adaptive
Target Courant number	0.3	—	0.3

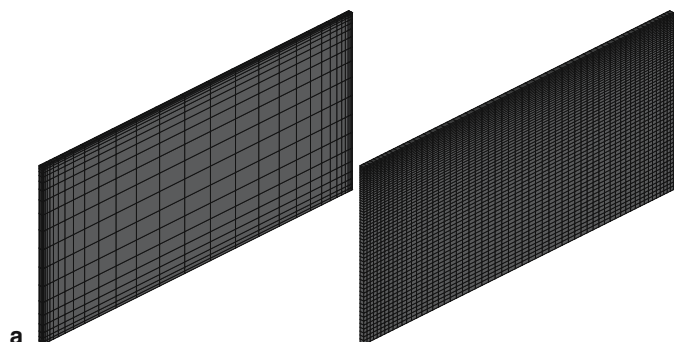


Fig. 9. Surface grid of the blade. **a** M12e4 mesh, **b** M14e5 mesh

volume fraction scheme, whatever the flow velocities.¹⁸ The second was performed on a much finer grid (M14e5) of 1 400 000 cells, but with a 0.005 s constant time step, which lead to Courant numbers locally larger than 0.3. The third simulation also used this fine grid, but with an adaptive time law. An insight into the mesh fineness can be seen in Fig. 9, which represents the surface grid on the blade. It can be noted on Fig. 9b that even if it contains 1 400 000 cells, the finest grid M14e5 has not so many small cells because the whole domain around the blade has to conserve small cells to capture the free surface precisely. This is because the free surface moves along the whole surface of the blade during the motion. Therefore, in quite a large area around the blade where the free surface is largely in motion, cells of small size have to be kept. In fact, without an automatic local adaptive mesh refinement, as has been detailed by Hay et al.,¹⁸ this feature is necessary to maintain a well-defined (i.e., not too diffused) interface during the whole stroke. A global view of the boundaries of the fluid domain (except the upper boundary) is shown on Fig. 10. The surface of the blade can be observed in the middle of the fluid domain. In fact, the blade is not positioned exactly in the middle because the motion is not symmetric. Figure 11a illustrates this point: it shows a horizontal slice of the mesh (fluid domain is vertically extruded). Figure 11b is a close-up of Fig. 11a around the blade. The boundary conditions are imposed as follows: on the top, a hydrostatic pressure is imposed, whereas a slip condition is required on the bottom of the domain (a hydrostatic pressure could also have been imposed here).

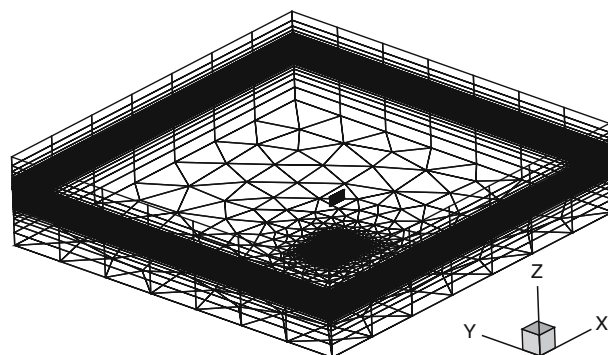


Fig. 10. Global view of the fluid domain (M14e5 mesh)

In the lateral regions, the velocity is imposed with its far-field value. For these first simulations, only a slip condition was tested on the blade, neglecting the turbulence effects around it. In this study, the Earth was chosen as the Galilean frame of reference. Hence, the translation of the carriage and the rotation of the blade are prescribed as an imposed motion of the blade (see Fig. 7) and the far-field velocity is then supposed to be at rest. Another possibility would have been to work in a Galilean frame linked to the carriage and to impose on the blade only the motion of rotation (and also a velocity equal to $V_b \vec{x}$ for the far field). But in the first case, the acceleration phase of the carriage can be reproduced more easily. Here, before launching the motion of rotation, a transient state for the motion of translation was used to raise smoothly the V_x component from zero up to the constant speed of the carriage. As detailed in Sect. 3.2, a rigid transformation of the mesh was favourably used: cells follow exactly the motion of the blade without deforming; the mesh quality is then conserved in time. The simulations exhibited the very complex evolution of the free surface. Figures 12–17 represent the free surface at different times in the blade frame. The (a) parts of the figures are viewed from the side away from the shaft, looking towards \vec{t} and blanking values on the \vec{t} axis lower than -1.458 m (the origin being set at point O, the centre of rotation of the oar, see Fig. 3). The centre of view of the (b) parts of the figures is located on the shaft side, looking towards the blade, and blanking values greater than -1.158 m, i.e., a quarter of the blade spanwise.

Fig. 11. Horizontal slice through the M14e5 mesh. **a** Top view, **b** close up of the region above the blade

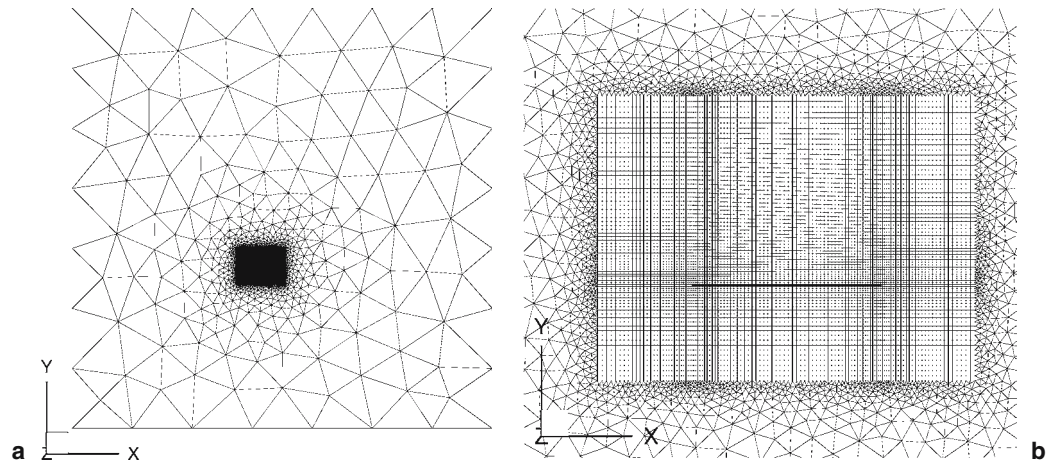


Fig. 12. Free surface at $t = 2.1$ s. **a** External view, **b** shaft view

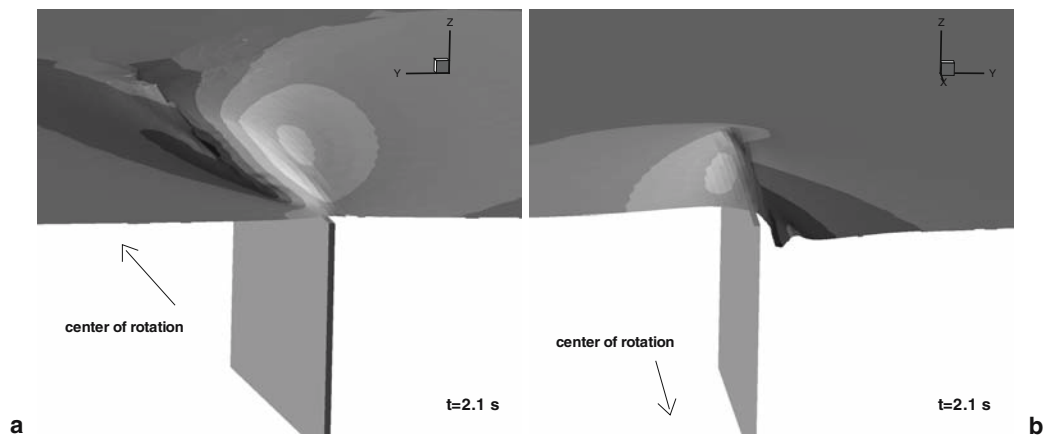
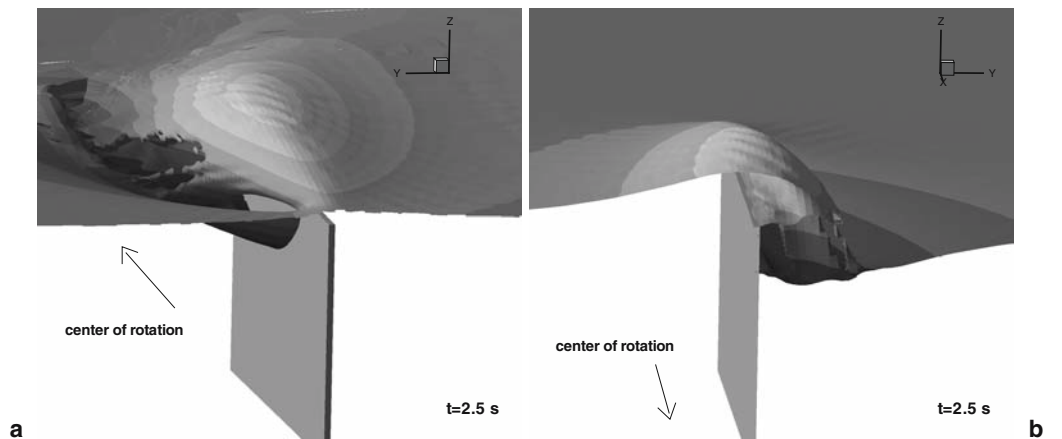


Fig. 13. Free surface at $t = 2.5$ s. **a** External view, **b** shaft view



At the beginning of the rotation, it can be observed in Fig. 12 that there is an elevation of the free surface just behind the inflow side of the blade, and consequently a flow passing over the upper part of the blade. Simultaneously, the low-pressure level generated on the other side of the blade leads to a bowl-shaped cavity

that increases in size. The cavity and the elevation become more intensified as time (and so θ) increases and the flow above the blade gradually takes the shape of a conical breaking wave (see Figs. 13, 14). It is noted that this conical wave points towards the external tip of the blade. The deformation is thus more accentuated

Fig. 14. Free surface at $t = 2.7$ s. **a** External view, **b** shaft view

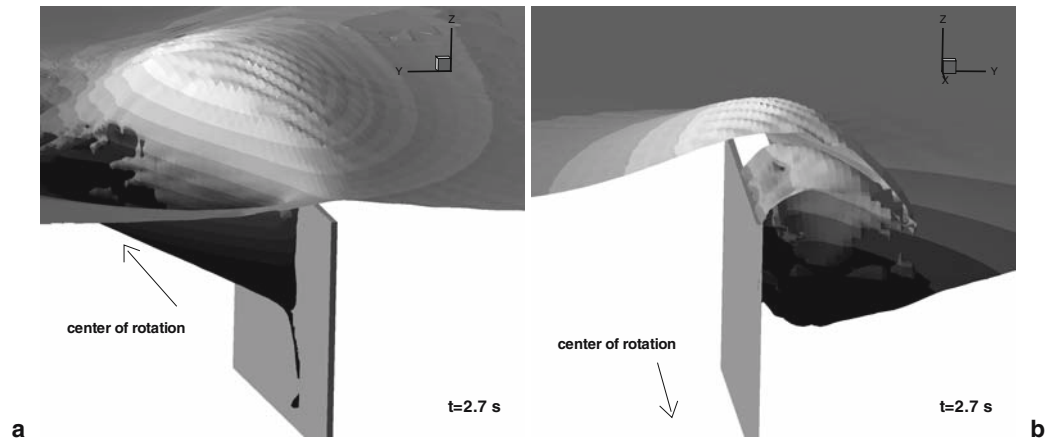


Fig. 15. Free surface at $t = 3.1$ s. **a** External view, **b** shaft view

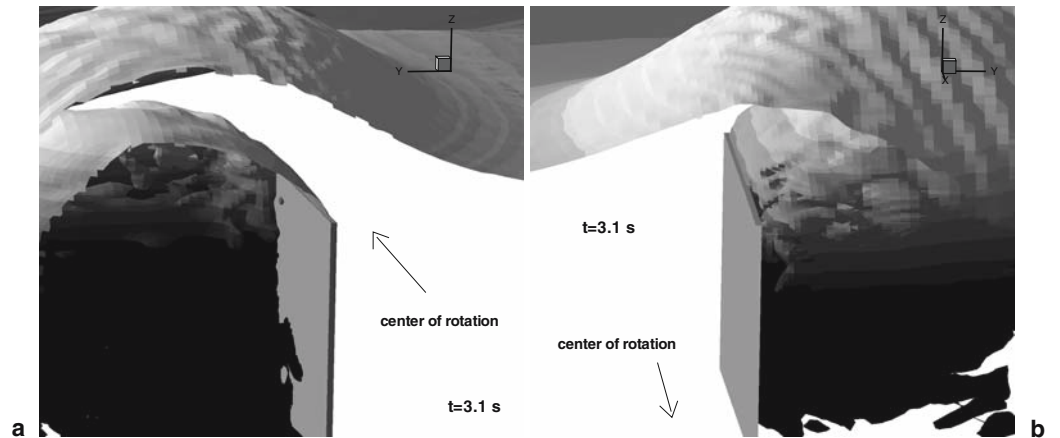
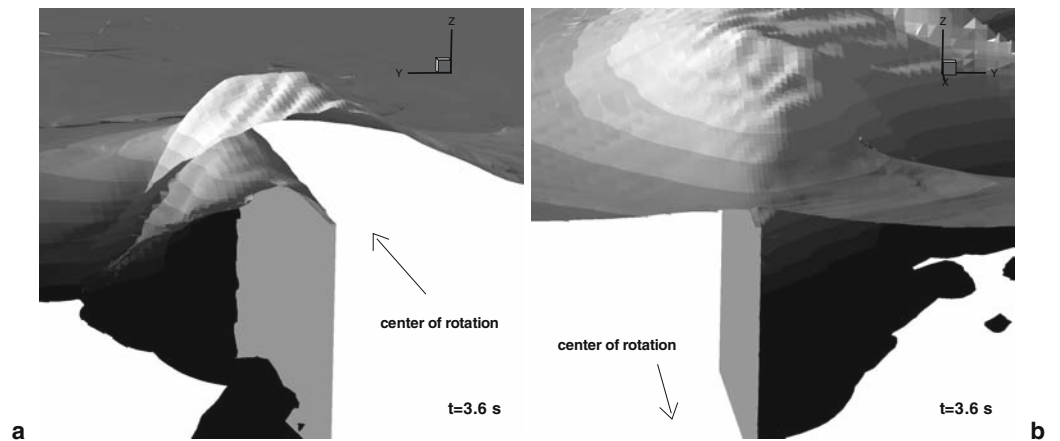


Fig. 16. Free surface at $t = 3.6$ s. **a** External view, **b** shaft view



in the part of the blade near the shaft. During the stroke, the free surface moves down to the bottom of the blade (see Fig. 15), generating a huge ventilated cavity. We can see here that the free surface seems to be more disturbed compared with a real rowing stroke. Videos of experiments (with a camera fixed to the shaft) tend to confirm this observation. This phenomenon is not so surprising since the efficiency η_0 used here ($=0.5887$)

is lower than that of real strokes, thus generating a more violent flow. In fact, the higher the efficiency, the less perturbed the flow is. The cavity is then convected (see Fig. 16) while the tip of the conical-shaped wave reverses its position with respect to the blade (now pointing towards the shaft). At the end of the motion (see Fig. 17), this flow pattern diminishes as the blade turns towards the flow direction.

Fig. 17. Free surface at $t = 3.9$ s. **a** External view, **b** shaft view

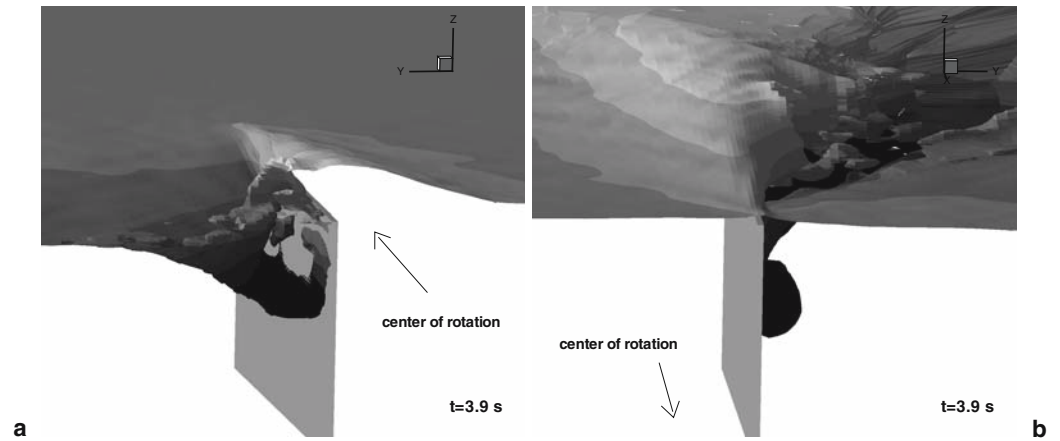
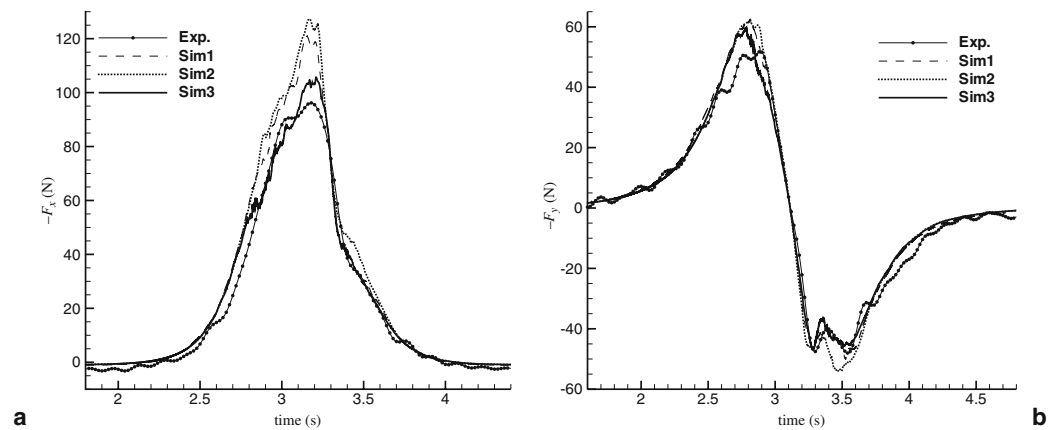


Fig. 18. Temporal evolution of the hydrodynamic force acting on the blade. **a** F_x component, **b** F_y component



4 Comparison with experimental data

Figure 18 compares the temporal evolution of the longitudinal and transversal forces from the experimental measurements and the results of the three simulations. First, looking at the period before the rotation is significant (and at the end of the stroke), we can see that the simulation gives lower drag in the x -direction. This is not surprising, since the motion of the blade is like that of a flat plane moving straight ahead (due to the translation of the carriage) in this part of the stroke. At this stage, the viscous drag acting on the blade is much larger than the pressure drag. But, because a slip condition is imposed on the blade, the viscous drag is not taken into account (calculated forces are mainly due to the pressure contribution), which explains the observed discrepancy.

Focusing on the F_x component, which represents the propulsive force, it can be seen that the Sim3 simulation gives better trends compared to the two others. This is very encouraging because Sim3 is the simulation with the finest grid using an adaptive time step leading to activation of the compressive properties for the numerical

scheme applied to the discretization of the volume fraction transport equation. Even if grid independence is unlikely to be achieved, the time evolution of forces is quite encouraging. In fact, the maximum value of F_x is closer to the experimental value and is quite well reduced compared to Sim1 and Sim2. The time evolution is also better reproduced, even if it is not in total agreement. But Sim3 is the only simulation able to capture an inflexion at about $t = 2.85$ s. Experimentally, this phenomena seemed to be found earlier at $t = 2.65$ s. This time discrepancy might be explained by the turbulence effect of the dynamics of the flow, especially at those angles where a dynamic stall occurs. This latter point is perhaps even more visible in Fig. 19a, in which the longitudinal forces are plotted as a function of the angle: an experimental break is visible at about 25° , whereas the same phenomenon seems to appear later numerically (at about 45°). Similar conclusions can be drawn on the F_y component (see Figs. 18b, 19b), for which Sim3 gives better results. However, there remain differences for higher values of F_y , obtained between $t = 2.65$ s and $t = 2.85$ s, i.e., between $\theta = 25^\circ$ and $\theta = 50^\circ$. Surprisingly, it is noted that during the last part of the stroke, the evolu-

Fig. 19. Hydrodynamic force on the blade as a function of the angle of rotation θ . **a** F_x component, **b** F_y component

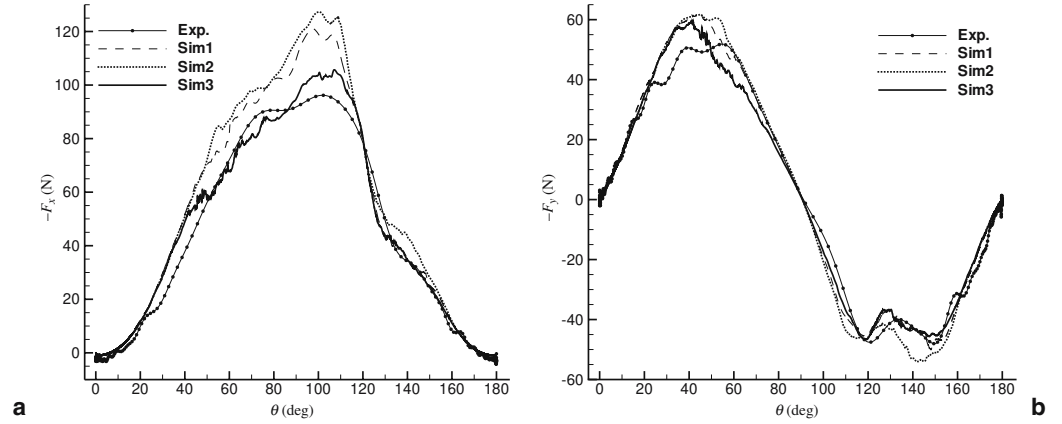
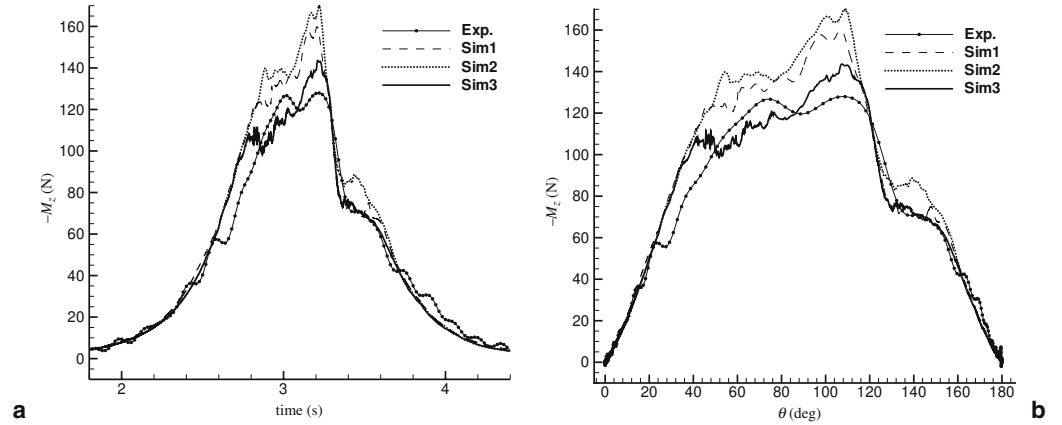


Fig. 20. Hydrodynamic z -axis torque (M_z) on the blade at point O . **a** M_z as a function of time, **b** M_z as a function of angle



tion is very well captured, especially when the forces stop decreasing at about $t = 3.3$ s. Comparison of the z -axis torque shows similar behaviour. Fairly good agreement is observed, apart from the angular zone between 25° and 50° . Here again, it seems that the break observed in the measured increase of M_z at $\theta = 25^\circ$ and $t = 2.65$ s occurs about 0.2 s later in the simulation. In conclusion, we can say that the phenomenon observed experimentally at $t = 2.65$ s, (which results in a break on the evolution of forces F_x and F_y), is not yet accurately captured by the simulations. In fact, it seems to occur later numerically (for the more precise simulation Sim3). These differences could perhaps be explained by too coarse a grid even on the M14e5 mesh and also by the influence of the turbulence effect on pressure and then on the free-surface elevation, especially when a dynamic stall occurs. It can also be noted in Fig. 6 that, after $t = 2.6$ s (up to $t = 3.0$ s), the difference between the analytical law (θ_a) prescribed by the simulation and the real measured angle (θ_m) varies rapidly. It locally leads to a difference of about 0.4° s^{-1} for the angular velocity, which is surely too small to explain the observed gap between the measured and simulated forces.

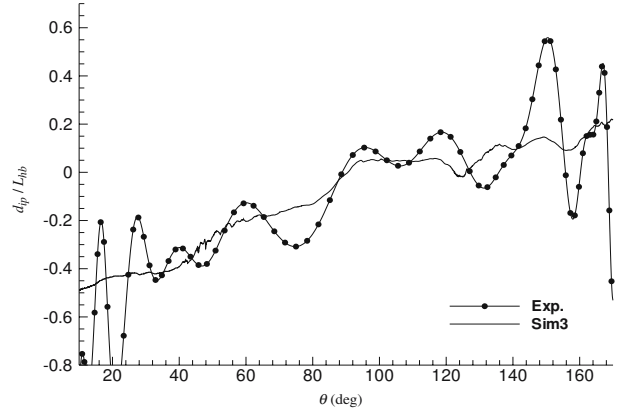


Fig. 21. Evolution of the d_{ip}/L_{hb} ratio

Figure 21 plots the quantity d_{ip} over half a blade length (denoted by L_{hb}). As point P is the localization where the resultant force acts, this figure shows that the migration of this point towards the shaft of the blade is accurately calculated. Finally, Figs. 22 and 23 concern the efficiencies. At the beginning of the stroke, it can be seen that the main difference between η and η_0 is mainly

Fig. 22. Evolution of efficiencies η_f (a) and η_p (b). The efficiencies are defined in Eq. 5

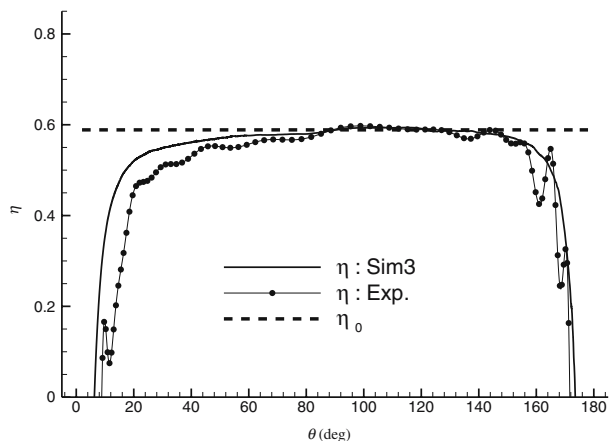
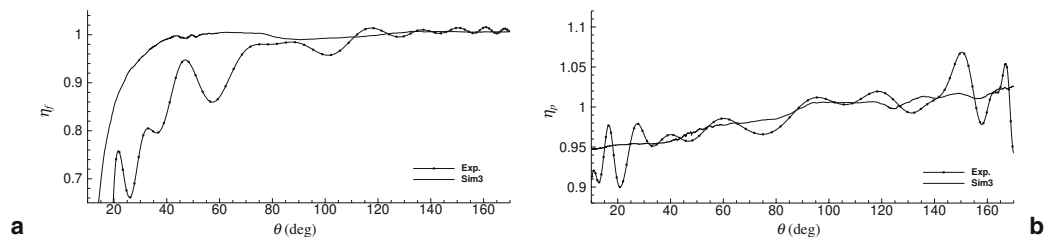


Fig. 23. Comparison of efficiency η with respect to η_0

due to η_f , i.e., the orientation of the hydrodynamics with respect to the perpendicular direction of the blade. As Eq. 5 shows, this orientation has all the more influence on η as θ deviates from $\pi/2$. For the range of angles corresponding to the first part of the stroke (just after the catch), β is negative, i.e., the orientation of the force is unfavourable for propulsion. The propulsion is then lower than if the force were directed along \vec{n} . The difference between the simulation and experiment here is found to result from quite a large discrepancy in η_f in the first part of the stroke, whereas the evolution of η_p is in good agreement with measurements. As noted previously, the position of point P is actually well captured by the simulation. It is also seen that this coefficient η_p remains close to 1 during a large part of the stroke ($\eta_p \in [0.94, 1.01]$ for $\theta \in [40^\circ, 140^\circ]$).

Figure 23 finally shows that η_0 can actually be considered the dominant parameter for such a stroke between $\theta = 40^\circ$ and $\theta = 140^\circ$, corresponding to the effective propulsive phase for oarsmen. Here again, quite a large gap between the experimental and numerical efficiency η is visible in the first part of the stroke (mainly due to the component η_f , as remarked previously). For angles less than about 20° , the difference is quite large, because the viscous contribution to F_x (which cannot be captured by the simulation since a slip condition is imposed on the blade) remains quite large compared to

the pressure effect. In contrast, it does not influence F_y similarly since the latter is mainly produced by the pressure effect when θ is small. As a result, the angle β (and so η_f) cannot be precisely evaluated in this case.

5 Conclusions

The flow around an oar blade is very complex, especially because a human is part of the system. From the hydrodynamics point of view, it is an unsteady 3-D flow including violent free-surface motion and overturning. From the kinematics point of view, the motion of the blade results in a variable translation of the boat coupled to a rotation of the shaft and a vertical movement of the blade (even if in the present analysis, the latter is not taken into account). To investigate the flow and to improve the modelling of the forces acting on a blade (as part of a simulator for a complete boat-oarsmen-oars system), a device reproducing a simplified rowing stroke was designed and built. The chosen kinematics are not excessively restrictive and give a reliable database to validate the numerical approach. The numerical simulations presented here demonstrate the capacity to deal with such a complex flow, especially since the present work uses a low-efficiency movement that produces a more violent flow than that of a real rowing stroke. Even if grid convergence is not obtained and turbulence is not yet taken into account, comparisons with experimental data are very encouraging and give confidence in the capacity of the numerical method to simulate accurately such a flow pattern. The fact that the elevation and the shape of the free surface extensively change during the stroke makes the task more difficult. As a matter of fact, the whole part of the domain in which the interface takes place has to be gridded with fine cells. Without a local adaptive grid procedure, meshes with a huge number of cells are needed and simulations are hampered by a lot of useless fine cells. As has already been found by Hay et al.,^{18,19} the development of a fully parallelized local mesh refinement procedure with dynamic load balancing should decrease dramatically the processing time, while keeping the generality of the approach. With this technique,

accurate simulations might be performed within a reasonable time. When this technique is operational and the processing time far shorter, new simulations will be performed for other experimental data of an oar with a rigid shaft. Comparisons with available data from real oars realized with the experimental device could also be added. Then, it will be possible to study the influence of oar deformation. Once simulations are validated with these towing tank tests, numerical simulations for a realistic configuration will be relevant and will become far easier than experimental approaches. Indeed, the study of complex movements with variable immersion (with catch and finish) and with a variable speed of translation taken into account will become much easier than carrying out tests experimentally. The last step will then be validation by real rowing tests, which we have been carrying out for several years with instrumented oars and measurement equipment on the boat to record the oar and oarsman kinematics. With the numerical results of parametric studies on oars (e.g., stiffness, lever length, and shape of the blade) and movement characteristics, we will be able to replace empirical indications by objective and unbiased criteria not only for oars but also for the rowing style. Furthermore, a detailed analysis and comparison of the flow topology for some selected and typical results could then be started to precisely understand the physical mechanism involved in such a complex configuration. The knowledge gathered in these fields and from such models as a result of these studies will be then progressively integrated into the global simulator.

Acknowledgments. The authors gratefully acknowledge the scientific committee of CINES (project dmn2049) and IDRIS (project 0129) for the attribution of computer time.

References

1. Wellicome JF (1967) Some hydrodynamic aspects of rowing. In: Williams JGP, Scott AC (eds) Rowing, a scientific approach. Barnes, New York
2. Videv TA, Doi Y (1993) Unsteady viscous flow simulation around the blade of a rowing boat. *J Soc Naval Archit Jpn* 173:97–108
3. Barré S, Kobus JM (1998) New facilities for measurement and modelling of hydrodynamic loads on oar blades. In: Haake SJ (ed) *The engineering of sport*. Blackwell
4. Pope DL (1973) On the dynamics of men and boat and oars. In: Bleustein JL (ed) *Mechanics and sport*. ASME, New York, pp 113–130
5. Barré S (1998) Etude expérimentale des systèmes de propulsion instationnaire. Application aux palettes d'aviron. PhD Thesis, University of Nantes/Ecole Centrale de Nantes, France
6. Spalart PR, Allmaras SR (1992) A one-equation turbulence model for aerodynamic flows. *AIAA 30th Aerospace Sciences Meeting*. Reno, NV, AIAA Paper 92-0439
7. Menter FR (1993) Zonal two-equation $k-\omega$ turbulence models for aerodynamic flows. *IAIAA 24th Fluid Dynamic Conference*. Orlando, FL, AIAA Paper 93-2906
8. Duvigneau R, Visonneau M, Deng GB (2003) On the role played by turbulence closures for hull shape optimization at model and full scale. *J Mar Sci Technol* 8:11–25
9. Jasak H, Weller HG, Gosman AD (1999) High-resolution NVD differencing scheme for arbitrarily unstructured meshes. *Int J Numer Methods Fluids* 31:431–449
10. Pržulj V, Basara B (2001) Bounded convection schemes for unstructured grids. In: *Proceedings of the AIAA 15th computational fluid dynamics conference*. Anaheim, CA, AIAA paper 2001-2593
11. Jasak H, Weller HG (1995) Interface tracking capabilities of the inter-gamma differencing scheme. Internal report, CFD research group, Imperial College, London
12. Leonard B (1988) Simple high-accuracy resolution program for convective modelling of discontinuities. *Int J Numer Methods Fluids* 8:1291–1318
13. Gaskell PH, Lau AKC (1988) Curvature compensated convective transport: Smart, a new boundedness-preserving transport algorithm. *Int J Numer Methods Fluids* 8:617–641
14. Queutey P, Visonneau M (2007) An interface-capturing method for free-surface hydrodynamic flows. *Comput Fluids* 36:1481–1510
15. Leroyer A (2004) Fluid/motion interaction for solid and flexible bodies by resolution of the Navier–Stokes equations. Contribution to the numerical modelling of cavitating flows. PhD Thesis, University of Nantes/Ecole Centrale de Nantes, France. Can be downloaded (in French) at ftp://ftpa.ec-nantes.fr/pub/DMN/Thesis/these_leroyer.pdf
16. Ferziger JH, Perić M (2002) *Computational methods for fluid dynamics*, 3rd edn. Springer-Verlag, Berlin
17. Leroyer A, Visonneau M (2005) Numerical methods for RANSE simulations of a self-propelled fishlike body. *J Fluids Struct* 20:975–991
18. Hay A, Leroyer A, Visonneau M (2006) H-adaptive Navier–Stokes simulations of free-surface flows around moving bodies. *J Mar Sci Technol* 11:1–18
19. Hay A, Visonneau M (2005) Computation of free-surface flows with local mesh adaptation. *Int J Numer Methods Fluids* 49:785–816